Original Article

Institution of MECHANICAL ENGINEERS

Journal of SYSTEMS AND CONTROL ENGINEERING

Proc IMechE Part I:
J Systems and Control Engineering
1–14

DOI: 10.1177/0959651819871783
journals.sagepub.com/home/pii
SAGE

Feedback controller designs for an electromagnetic micromanipulator

Mustafa Böyük, Yakup Eroğlu, Günyaz Ablay and Kutay İçöz

Abstract

Magnetic micromanipulators are capable of generating wide range of magnetic forces to manipulate magnetic microparticles for biomedical applications. In this study, a multipole magnetic micromanipulator system including electromagnets, driver circuitry and control unit is designed, modeled and implemented. The micromanipulator can produce a broad range of magnetic forces up to 25 pN on a single magnetic microparticle (1–10 μm diameter) that is 5 mm away from the electromagnet core tip. Both linear and nonlinear controllers are designed and implemented, and the proposed nonlinear controller produces smooth control currents to assure closed-loop stability of the system with 1 s non-overshoot transient response and zero steady-state tracking error. The maximum output current of the driver circuitry is set to 1 A. The single particle at the center is moved at a speed of 5 mm/s. The fully automatic system can be utilized in applications related to single cell or microparticle manipulations.

Keywords

Micromanipulation, magnetic manipulator, magnetic force, modeling, nonlinear control

Date received: 15 May 2019; accepted: 4 August 2019

Introduction

Manipulation of the magnetic microparticles has been drawing great attention in recent years due to wide range of applications in biology and medicine.[1–7] The most commonly used microparticles are made from superparamagnetic or ferromagnetic core materials. These particles are commercially available in sizes ranging from 0.2 to 100 μm and are conjugated with specific antibodies or chemicals to make them functional for various applications.[8–10] Under external magnetic field, the magnetic microparticles can be remotely manipulated as a non-invasive tool for cell manipulation,[11] DNA–RNA extracting,[12] immunoassays,[13] targeted drug delivery,[14–16] magnetic resonance imaging,[17] hyperthermia therapies[18,19] and signal amplification.[20] Magnetically controlled drug delivery is one of the significant methods among the targeted treatment systems.[21] Magnetic particles with conjugated drugs are used to reach to the targeted region properly and deliver the drug for cancer treatment.[22–24] Another application involving magnetic microparticles is magnetic separation where magnetically labeled entities are removed from the nonmagnetic medium. With this approach, the extraction of tumor cells and separation of specific enzymes were achieved.[25] Magnetic particles have been also used for therapeutic purposes. Recently, the treatment of small or deep-seated tumors was achieved by heating of the targeted regions, known as hyperthermia.[19,26]

For manipulation of magnetic particles, the required external magnetic field is usually generated by permanent magnets or electromagnets.[25,27,28] Compared with the other micromanipulation methods such as optical tweezers[29] and atomic force microscopy,[30] the magnetic manipulators have much wider application areas, they do not damage the biological entities and are easy to use.[6,31,32] The magnetic manipulators including the permanent magnets are designed with some empirical calibrations and useful for simple magnetic tweezer applications such as analysis of the DNA molecule topology and topoisomerases studies.[6,33–35] The electromagnet-based designs provide some diverse construction alternatives by controlling the amplitude and the direction of the magnetic force.[1] Some applications include measurement of adhesion strength,[36]

Department of Electrical and Electronics Engineering, Abdullah Gül University, Kayseri, Turkey

Corresponding author:
Günyaz Ablay, Department of Electrical and Electronics Engineering, Abdullah Gül University, Kayseri 38080, Turkey.
Email: gunyaz.ablay@agu.edu.tr

investigation of receptor binding firmness,[37] torque generations,[38] magnetically driven microrobotic systems[39–41] and some industrial applications.[42]

In this study, an electromagnet-based magnetic micromanipulator system for controlling microparticles in a fluidic environment is designed, modeled and controlled. The micromanipulator is designed using finite element–based numerical solvers for optimal magnetic force generations. At present, in the literature, the research scholars have mostly focused on actuating 0.1-to-10-mm-sized magnetic particles; the modeling methods of the magnetic actuation systems are based on the general magnetic force models, and thus there is no systematic control approach. In this work, a quadrupole magnetic micromanipulator system is developed for manipulating magnetic microparticles in the range of 1–10 μm diameter. For control and analysis purposes, a current-to-force relation–based model for the magnetic micromanipulator system is derived from the first principles–based modeling in which the magnetic monopole and magnetic circuit techniques are incorporated. A systematic nonlinear controller based on the integral backstepping approach with smooth control outputs is proposed for automatic control of the magnetic micromanipulator. The performance of the nonlinear controller is compared to that of an offset current–based linear controller, and the experimental results are given to demonstrate the viability and efficacy of the proposed controllers.

System description and design

In this study, a quadrupole magnetic micromanipulator system is put into practice, mathematically modeled, analyzed and automatically controlled. The system configuration is illustrated in Figure 1. The magnetic micromanipulator system is composed of multiple electromagnetic actuators, a microfluidic workspace, an imaging system consisting of a camera and an objective, a workstation, a microcontroller, a power interface circuit, a multichannel DC power supply and a Cartesian manipulator. By virtue of COMSOL Multiphysics, the electromagnets are composed of 2000 copper winding on a nickel–iron alloy core whose length is of 76 mm. The ferromagnetic Ni-Fe alloy strengthens the electromagnets for generating adequate magnetic forces to manipulate the microparticles in a fluidic medium. The Ni-Fe alloy is preferred because of its good magnetic permeability features, high magnetic saturation figure and low cost.[43] Each of the cores is fixed with plastic clamps on the plexiglass to prevent any unbalanced situation that stems from the magnetic pulling force of each electromagnet. It is seen in Figure 1 that four electromagnets are designed and placed symmetrically in order to manipulate the microparticle in x–y directions. The workspace (or fluidic reservoir) is made of poly(methyl methacrylate) (PMMA) (plexiglass) with a 10 mm diameter, and it is located at the center of the electromagnets. The PMMA material is selected because it is transparent and can be shaped easily using the laser cutter. Camera-objective system is used to detect the magnetic microparticle in the fluidic reservoir. The industrial USB 2.0 complementary metal oxide semiconductor (CMOS) camera is able to capture 53 frames per second with a 640 × 480 pixel resolution. A 10× objective is used to magnify the microparticles in the workspace. The motorized Cartesian manipulator is used for adjusting the position of the camera setup in x–y–z

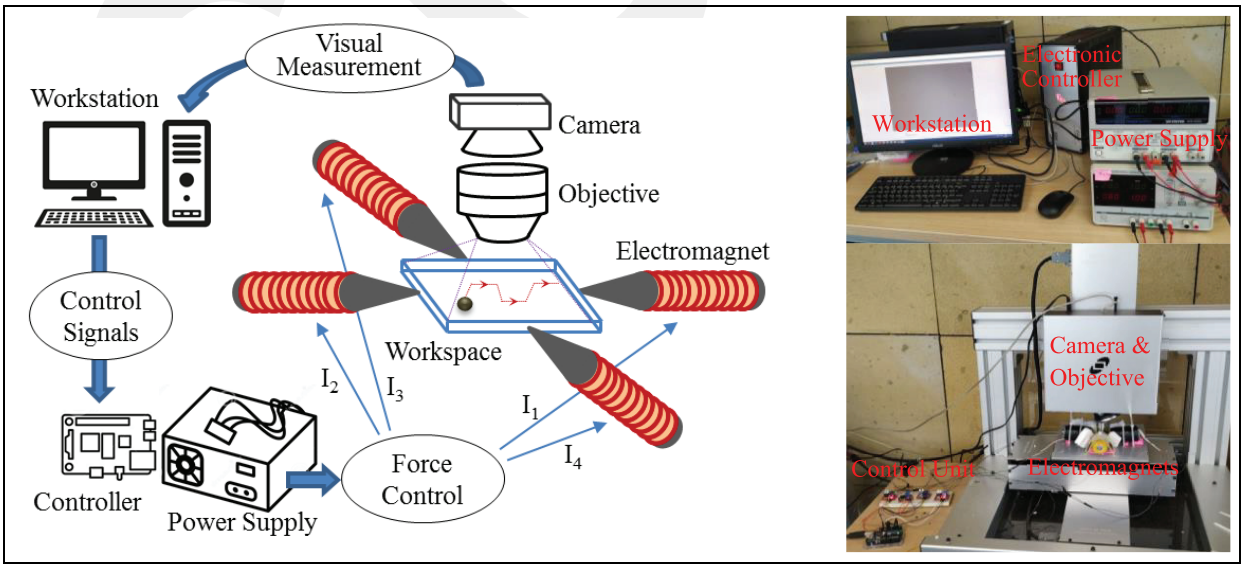

Figure 1. A quadrupole magnetic micromanipulator system and its experimental setup.

directions. The current needs of electromagnets are solved with a multichannel DC power supply that provides 0–30 V adjustable voltage outputs and 0–3 A adjustable current outputs. The pulse width modulation (PWM) outputs of a microcontroller are interfaced with power MOSFET driver circuits to deal with the varying current needs of the electromagnets. A powerful workstation equipped with MATLAB software is used for data acquisition and video processing in real time. Based on the video images, an online particle identification and tracking algorithm are established for detecting the microparticle position and using it in the feedback control algorithms.

One of the most critical aspects of the system is related to design of magnetic micromanipulators. To get optimal actuator designs, the magnetostatic problem of the magnetic micromanipulators can be solved with numerical or analytical techniques. Analytical methods including the Biot–Savart law may be implemented to get solutions, but the complexity of the geometry and usage of different materials makes such analytical solutions cumbersome. Thus, we used finite element–based numerical solvers to solve the magnetostatic design problem. In our previous work,[1] we reported the details of the electromagnet design for one axis system. In this work, COMSOL Multiphysics software is used for two-axes (two-dimensional (2D)) design, in which it provides finite element–based solutions to partial differential equations of the magnetostatic problem. The equations of the magnetostatic problem are given by

$$\vec{B} = \nabla \times \vec{A},\ \nabla \times \vec{H} = \vec{J} \tag{1}$$

where B, A, H and J represent the magnetic flux density, magnetic vector potential, magnetic field intensity and current density, respectively. The current density is defined by

$$\vec{J} = \sigma \vec{E} + \vec{J}_e,\ J_e = \frac{NI_c}{A_c} \tag{2}$$

where σ is the electrical conductivity, E is the electric field intensity, N_c is the number of coil windings, I_c is the total coil current and A_c is the total cross-section area of the coil domain. From solutions of magnetic vector potential, A, the COMSOL evaluates the magnetic field B and its elements in a given region. Some of the COMSOL-based design results are illustrated in Figure 2. Since the produced magnetic force heavily

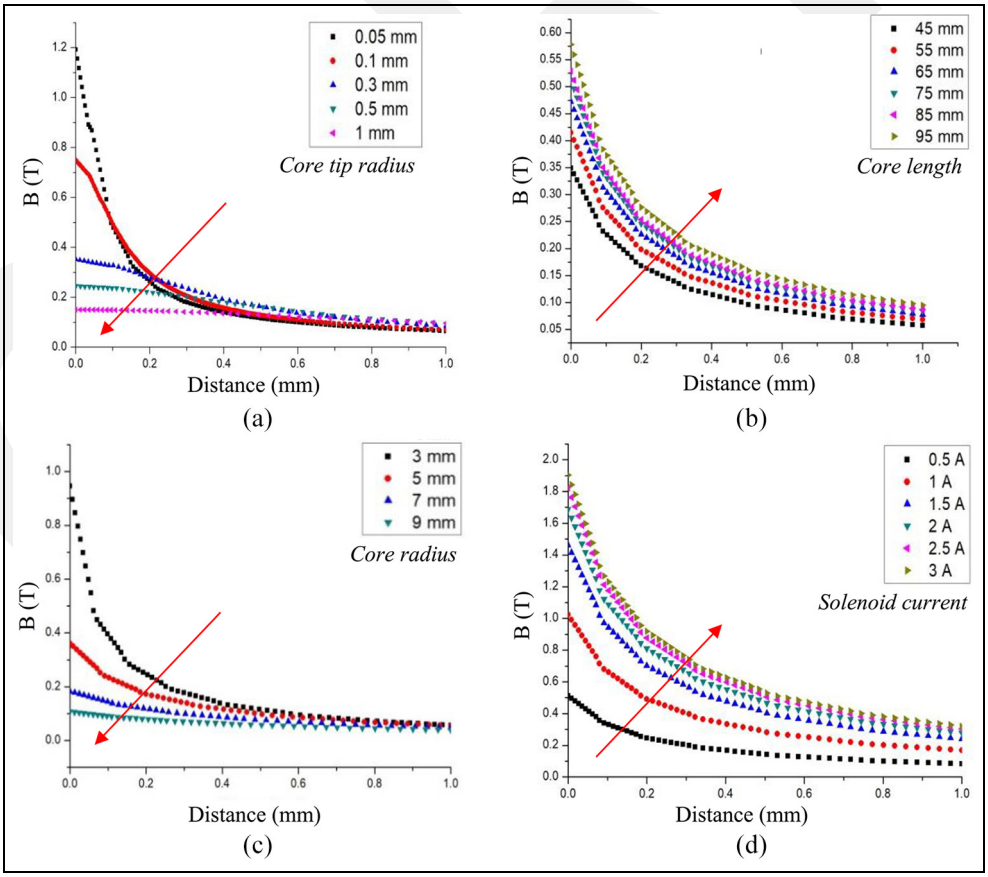

Figure 2. Magnetic flux density variations with (a) core tip radius, (b) core length, (c) core radius and (d) solenoid current (arrow shows the trend).

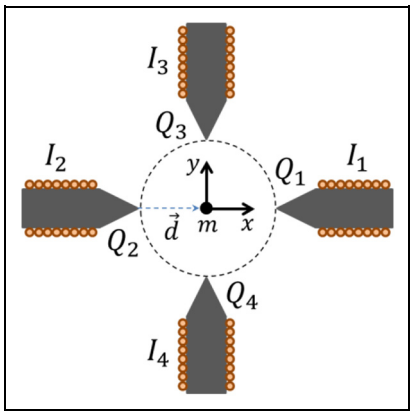

Figure 3. A representation of the magnetic micromanipulator for modeling.

depends on the geometry and core materials, to exert an adequate magnetic force on a single magnetic microparticle, sharp and roller-shaped core tip geometry is designed. In order to find optimal magnetic field solutions, many parameters such as core radius, core length, tip radius, taper length, solenoid current, solenoid position and permeability of the material have been taken into account. Figure 2(a) shows the magnetic flux density distribution when the radius of core tip varies. It is seen from the figure that magnetic flux density decreases with increasing radius of the core tip. Sharper core tips yield intense magnetic field density and high field gradient; however, the magnetic force diminishes rapidly with increasing distance. It should be noted that the magnetic flux density lessens with distance with $\sim d^3$ in diamagnetic surroundings. Figure 2(b) displays magnetic flux distribution when the core length varies. The magnetic flux density increases with increasing core length (i.e. the longer the core length is, the stronger the magnetic field is). Figure 2(c) shows the effect of the core diameter on the flux density, which decreases with increasing core diameter. Figure 2(d) illustrates the effect of the solenoid current on the magnetic field generation. The magnetic flux density increases with the applied current until the material reaches magnetic saturation. All these features are taken into account for selection of optimal design parameters in the design of electromagnets.

While the numerical solvers are utilized for getting optimal magnetic actuator designs in terms of geometry and materials, the first principles approach is needed to model the system for achieving analysis, calibration and suitable control designs.

Equations of motion for magnetic microparticles

The system can be partitioned into particle dynamics and electrical dynamics, and modeled with the first principles approach. Consider the quadrupole electromagnetic actuator as illustrated in Figure 3, the dynamics of the microparticle whose mass is m can be modeled with Newton's second law, and the electromagnets can be modeled with Kirchhoff's voltage law. Then, the interaction between these models can be combined via magnetic force model to complete the modeling.

The magnetic microparticle dynamics in an aqueous environment is obtained by applying Newton's second law of motion. Various forces that are subject to microparticle dimension, and working surroundings have impact on the movement of microparticles. For the magnetic microparticles, whose radius is about 0.5–5 μm, the most dominant forces are the magnetic force, the friction force and the drag force.[44] Thus, the dynamics of motion of the magnetic microparticle in x and y directions can be written as

$$\begin{aligned} m\ddot{x} + F_{vx} &= F_{mx} + F_d \\ m\ddot{y} + F_{vy} &= F_{my} + F_d \end{aligned} \tag{3}$$

where m(in kg) is the mass of microparticle, F_{vx} and F_{vy} are the friction forces, F_{mx} and F_{my} are the applied magnetic forces, and F_d (in N) represents the random disturbance affecting the magnetic microparticle. The friction forces, F_{vx} and F_{vy}, are given by

$$F_{vx} = \rho\dot{x}\,,\; F_{vy} = \rho\dot{y} \tag{4}$$

where, as stated by Stokes' law,[45] the drag coefficient ρ(in Ns/m) is defined by $\rho = 6\pi\theta\alpha h$: θ, α and h are the fluid viscosity, correction coefficient and particle radius, respectively.

The microparticle is controlled with the magnetic forces F_{mx} and F_{my} which are generated by the electromagnets. The magnetic force responsible for the movement of the magnetic microparticle is related to the magnetic flux B(in T) and the magnetic moment function m(in Am^2), and can be written in any direction as[46]

$$\vec{F}_m = \frac{\nabla\left(\vec{m}\cdot\vec{B}\right)}{2} \tag{5}$$

The magnetic dipole moment for a weak magnetic microparticle is defined by Shevkoplyas et al.[47]

$$\vec{m} = \frac{3V_b}{\mu_0}\frac{(\mu-\mu_0)}{(\mu+2\mu_0)}\vec{B} \tag{6}$$

where V_b is the volume of the particle, μ is the magnetic permeability of the particle and μ_0 is the magnetic permeability of the free space. By substituting equation (6) into equation (5), the magnetic force can be obtained as

$$\vec{F}_m = k_f\nabla\left(\vec{B}\cdot\vec{B}\right) \tag{7}$$

where $k_f = 3V_b(\mu-\mu_0)/(2\mu_0(\mu+2\mu_0))$. This form of the magnetic force equation completely depends on the

spatial coordinates. However, the magnetic force can be calculated by specifying the magnetic field (B) so that a suitable control algorithm can be generated. If the pole (or core) tip is assumed as a point magnetic charge, the produced magnetic field at a coordinate position $\vec{d}$ can be written as

$$\vec{B} = k_m \frac{Q}{d^2} \hat{r} \tag{8}$$

where $\hat{r} = \vec{d}/d$ is unit directional vector, $\vec{d}$(in m) represents magnetic microparticle position, Q(in Am) represents the magnetic charge and $k_m = \mu_0/4\pi$ is the magnetic field constant. In order to calculate the magnetic force, Q must be determined. The magnetic charge Q is a function of the magnetic flux ϕ defined by $Q = \phi/\mu_0$. Using Ampere's loop law, the magnetic flux can be obtained by $\phi = N_c I/R_a$: where N_c is the number of coil windings, R_a represents the magnetic reluctance, known as $R_a = g_a/(\mu_0 A_a)$, where $\mu_0 = 4\pi \times 10^{-7}$(in Tm/A), g_a(in m) is the gap between pole tip and particle, and the cross-sectional area is given by A_a(in m^2). Finally, by writing equation (8) into equation (7), the magnetic forces at the workspace center ($x = 0$, $y = 0$) are obtained as[1]

$$\begin{aligned} F_{mx} &= k_{fm}\left(I_1^2 - I_2^2\right) \\ F_{my} &= k_{fm}\left(I_3^2 - I_4^2\right) \end{aligned} \tag{9}$$

where

$$k_{fm} = \frac{4N_c^2 k_f k_m^2}{\mu_0^2 R_a^2 d^5} \tag{10}$$

where d(in m) is the radius of workspace (or the distance from the tip of the coil to the magnetic microparticle). Now, the generated magnetic forces are represented with the control currents, which eliminate the spatial dependence of the magnetic force calculations.

The disturbing force F_d is composed of random thermal noise force and other forces such as particle interaction, thermophoretic, magnetic interaction and electrostatic interaction forces. However, the disturbing force F_d is mainly composed of random thermal noise force. The thermal noise force, or Brownian force, occurs on account of the influence of the liquid nanomolecules on the magnetic microparticle. The power spectrum of thermal noise force is given by $P(F_d) = 4k_b T\rho$, in which $k_b = 1.38 \times 10^{-23}$(J/K) refers to the Boltzmann factor and T(K) represents the temperature.[48] Moreover, the model mode of the thermal force is given by the white noise as[49]

$$F_d = \delta\left(\frac{2\rho k_b T}{T_s}\right)^{1/2} \tag{11}$$

where white noise δ has zero average and unit variance, and T_s refers to a sampling time. It should be noted that the magnetic force and the friction force are the most dominant forces for magnetic particles whose diameter is around 1–10 μm,[44] so the disturbing force has a negligible effect on the system in micrometer range. In addition, dynamic behavior of electromagnets (for $i = 1, 2, 3, 4$) can be modeled by

$$\frac{dI_i}{dt} = \frac{-R_e I_i}{L_e} + \frac{V_i}{L_e} \tag{12}$$

where L_e (H) is the magnet inductance, R_e (Ω) is the magnet resistance and V_i (V) is the supply voltage. The electromagnets are designed to be identical, so the electrical model parameters are practically the same. It should be noted that the electromagnet dynamics can be ignored in the control design and analysis since the electrical dynamics is much faster than the magnetic microparticle model dynamics. The time constant of the electromagnets is obtained as $\tau_e = L_i/R_i \approx 0.005$ s, which is almost 20 times faster than the overall system dynamics.

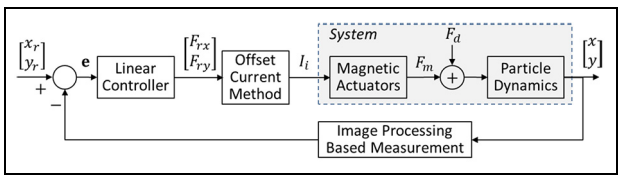

Figure 4. Block diagram of the linear control system.

Controller designs

In this section, linear and nonlinear feedback control systems are designed for accurate and rapid control responses.

Linear controller design

Since the system input is nonlinear, the first action may include linearization of the input currents via an offset current variable. As shown in Figure 4, the offset current approach can be used to reduce the control variables into one and then a linear controller can be designed to stabilize the magnetic micromanipulator system.

By considering equation (9), an offset variable I_0 and two control variables I_{c1}, I_{c2} can be defined such that the actual control currents become

$$\begin{aligned} I_1 &= \frac{I_0 + I_{c1}}{2}, I_2 = \frac{I_0 - I_{c1}}{2} \\ I_3 &= \frac{I_0 + I_{c2}}{2}, I_4 = \frac{I_0 - I_{c2}}{2} \end{aligned} \tag{13}$$

Substituting equation (13) into equation (9), the magnetic forces become

$$F_{mx} = k_{fm} I_0 I_{c1},\ F_{my} = k_{fm} I_0 I_{c2} \tag{14}$$

If I_0 is defined as a fixed variable and I_{c1}, I_{c2} are defined to be regulating variables, the magnetic force

can be practically implemented. For desired magnetic force variables, F_{rx} and F_{ry}, the control currents can be written as

$$I_1 = \frac{\left(I_0 + F_{rx}/\left(k_{fm}I_0\right)\right)}{2}, I_2 = \frac{\left(I_0 - F_{rx}/\left(k_{fm}I_0\right)\right)}{2}$$
$$I_3 = \frac{\left(I_0 + F_{ry}/\left(k_{fm}I_0\right)\right)}{2}, I_4 = \frac{\left(I_0 - F_{ry}/\left(k_{fm}I_0\right)\right)}{2} \tag{15}$$

By putting equation (15) into equation (3), the microparticle dynamics turns out to be

$$\begin{aligned} m\ddot{x} + \rho\dot{x} &= F_{rx} + F_d \\ m\ddot{y} + \rho\dot{y} &= F_{ry} + F_d \end{aligned} \tag{16}$$

Equation (16) shows that the closed-loop system dynamics are now linear, and the new control variables are the desired magnetic force variables, F_{rx} and F_{ry}. While various linear control forms can be considered for equation (16), since it is an integrating process, a basic proportional control law can be designed to stabilize the system dynamics

$$F_{rx} = k_{px}(x_r - x), F_{ry} = k_{py}(y_r - y) \tag{17}$$

where k_{px}, k_{py} are the proportional control gains, x_r, y_r are the fixed position references and x, y are the position measurements. By putting equation (16) into equation (17) and taking Laplace transform, the following transfer functions can be obtained

$$\begin{aligned} X(s) &= \frac{1}{ms^2 + \rho s + k_{px}}\left[k_{px}X_r(s) + F_d(s)\right] \\ Y(s) &= \frac{1}{ms^2 + \rho s + k_{py}}\left[k_{py}Y_r(s) + F_d(s)\right] \end{aligned} \tag{18}$$

From equation (18), it is clear that the closed-loop system is stable if $k_{px}, k_{py} > 0$. The linear controller design requires selection of three parameters, control gains k_{px}, k_{py} and offset variable I_0. The offset variable is an offset current that should be chosen with care not to reach magnetic saturation.

Nonlinear controller design

The goal is to design a suitable nonlinear state feedback controller that guarantees an asymptotically stable reference tracking performance. While the linear controller with offset current offers a simple controller, the nonlinear controller can be designed to improve control performance and to offer an alternative approach. The structure of the controlled system is illustrated in Figure 5. An integral backstepping-based controller is designed to control the magnetic force by stabilizing the current inputs, and thus, it can control the magnetic microparticle effectively.

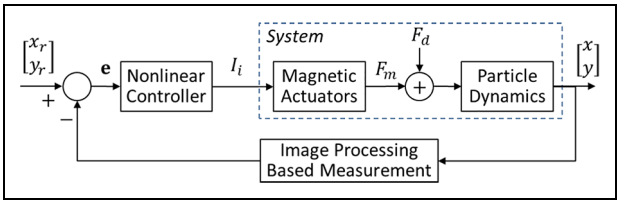

Figure 5. Block diagram of the proposed nonlinear control system.

Using equations (3) and (9), the model of magnetic micromanipulator system can be written as

$$\begin{aligned} \dot{x}_1 &= x_2 \\ m\dot{x}_2 &= -\rho x_2 + k_{fm}\left(I_1^2 - I_2^2\right) + F_d \\ \dot{y}_1 &= y_2 \\ m\dot{y}_2 &= -\rho y_2 + k_{fm}\left(I_3^2 - I_4^2\right) + F_d \end{aligned} \tag{19}$$

As stated before, the electrical dynamics, $G(s) = K_e/(\tau_e s + 1)$ (with $\tau_e = L_i/R_i \approx 0.005\,\text{s}$), are stable and much faster than the microparticle dynamics, so the possible dynamical influence of the electromagnet dynamics on the system performance can be neglected.

Lemma 1. For the system equation (19), define a controller

$$\begin{aligned} I_1^2 &= \frac{k_c\phi_1(u_1)}{k_{fm}}\ ,\ I_2^2 = \frac{k_c\phi_2(u_1)}{k_{fm}} \\ I_3^2 &= \frac{k_c\phi_3(u_2)}{k_{fm}}\ ,\ I_4^2 = \frac{k_c\phi_4(u_2)}{k_{fm}} \end{aligned} \tag{20}$$

where $k_c > 0$, the functions $\phi_1, \phi_2 \geqslant 0$ and $\phi_3, \phi_4 \geqslant 0$ are selected to satisfy $\phi_1(u_1) - \phi_2(u_1) = u_1$ and $\phi_3(u_2) - \phi_4(u_2) = u_2$ for all u_1, u_2, where u_1, u_2 are defined by equation (28). Then, the operating point (x_r, y_r) of the closed-loop system is stable.

Proof. Assume that x_r and y_r are fixed references, then define

$$\begin{aligned} e_1 &= x_1 - x_r \Rightarrow \dot{e}_1 = \dot{x}_1 = x_2 \\ e_3 &= y_1 - y_r \Rightarrow \dot{e}_3 = \dot{y}_1 = y_2 \end{aligned} \tag{21}$$

If x_2 and y_2 are viewed as the input stabilizing $\dot{e}_1$ and $\dot{e}_3$, then we can select $x_2 = -k_1e_1$ and $y_2 = -k_2e_3$. Since x_2 and y_2 are not inputs, define

$$e_2 = x_2 + k_1e_1\ ,\ \ e_4 = y_2 + k_2e_3 \tag{22}$$

From derivative of e_2, we get

$$\begin{aligned} \dot{e}_2 &= \dot{x}_2 + k_1\dot{e}_1 \\ &= \frac{\left[-\rho x_2 + k_{fm}\left(I_1^2 - I_2^2\right) + F_d\right]}{m} + k_1\dot{e}_1 \\ &= u_1 + k_1\dot{e}_1 - \rho x_2/m + F_d/m \end{aligned} \tag{23}$$

and similarly, from derivative of e_4, we get

$$\begin{aligned} \dot{e}_4 &= \dot{y}_2 + k_2\dot{e}_3 \\ &= \frac{\left[-\rho y_2 + k_{fm}\left(I_3^2 - I_4^2\right) + F_d\right]}{m} + k_2\dot{e}_3 \\ &= u_2 + k_2\dot{e}_3 - \rho y_2/m + F_d/m \end{aligned} \tag{24}$$

where u_1 and u_2 represent the auxiliary nonlinear control terms to be defined subsequently. Now, the model is transformed into the following error dynamics

$$\begin{aligned}\dot{e}_1 &= e_2 - k_1 e_1\\ \dot{e}_2 &= u_1 + k_1\dot{e}_1 - \rho\dot{e}_1/m + F_d/m\\ \dot{e}_3 &= e_4 - k_2 e_3\\ \dot{e}_4 &= u_2 + k_2\dot{e}_3 - \rho\dot{e}_3/m + F_d/m\end{aligned} \tag{25}$$

Here, define a positive definite Lyapunov function as

$$V = 0.5\left(e_1^2 + e_2^2 + e_3^2 + e_4^2\right) \tag{26}$$

Then, the time derivative of equation (26) is

$$\begin{aligned}\dot{V} &= e_1\dot{e}_1 + e_2\dot{e}_2 + e_3\dot{e}_3 + e_4\dot{e}_4\\ &= e_1(e_2 - k_1 e_1) + e_2(u_1 + k_1\dot{e}_1 - \rho x_2/m + F_d/m)\\ &+ e_3(e_4 - k_2 e_3) + e_4(u_2 + k_2\dot{e}_3 - \rho\dot{e}_3/m + F_d/m)\end{aligned} \tag{27}$$

Choose

$$\begin{aligned}u_1 &= \frac{k_{fm}\left(I_1^2 - I_2^2\right)}{m} = -\left(1 + k_1\rho/m + k_1^2\right)e_1\\ u_2 &= \frac{k_{fm}\left(I_3^2 - I_4^2\right)}{m} = -\left(1 + k_2\rho/m + k_2^2\right)e_3\end{aligned} \tag{28}$$

Then, we have

$$\begin{aligned}\dot{V} = &-k_1 e_1^2 - (\rho/m - k_1)e_2^2 + e_2 F_d/m - k_2 e_3^2\\ &-(\rho/m - k_2)e_4^2 + e_4 F_d/m\end{aligned} \tag{29}$$

where F_d is defined by white noise with zero mean ($E\{F_d\} = 0$), so its effect on the stability analysis is negligible, and if we define $0 < k_1 = k_2 = k < \rho/m$, then

$$\dot{V} < 0 \tag{30}$$

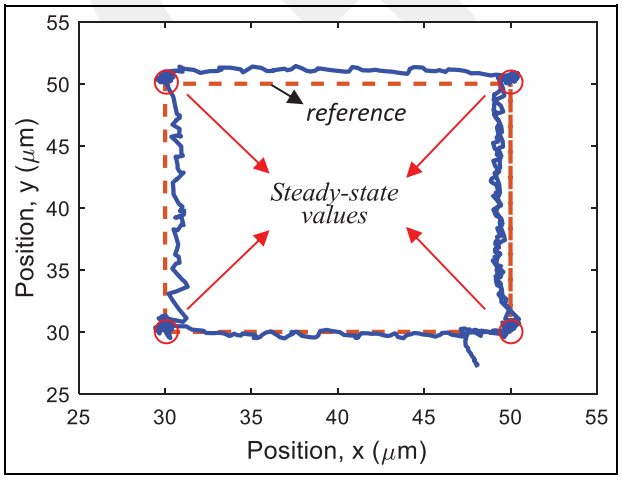

Figure 6. The phase-plane portrait of the system trajectories (x vs y) for step reference variations. The corners are the steady-state reference coordinates.

Hence, the controlled system has an asymptotically stable equilibrium point. This result is obtained by letting

$$\begin{aligned}I_1^2 - I_2^2 &= \frac{k_c[\phi_1(u_1) - \phi_2(u_1)]}{k_{fm}}\\ I_3^2 - I_4^2 &= \frac{k_c[\phi_3(u_2) - \phi_4(u_2)]}{k_{fm}}\end{aligned} \tag{31}$$

where $k_c > 0$, the functions ϕ_1, ϕ_2, ϕ_3 and ϕ_4 must be selected suitably to satisfy $\phi_1(u_1) - \phi_2(u_1) = u_1$ and $\phi_3(u_2) - \phi_4(u_2) = u_2$ for all u_1 and u_2. To have a smooth (differentiable) controller, a suitable choice can be

$$\begin{aligned}\phi_1(u_1) &= 0.5\left(u_1 + \sqrt{u_1^2 + \varepsilon}\right),\\ \phi_2(u_1) &= 0.5\left(-u_1 + \sqrt{u_1^2 + \varepsilon}\right)\\ \phi_3(u_2) &= 0.5\left(u_2 + \sqrt{u_2^2 + \varepsilon}\right),\\ \phi_4(u_2) &= 0.5\left(-u_2 + \sqrt{u_2^2 + \varepsilon}\right)\end{aligned} \tag{32}$$

where ε is a small positive number and

$$\begin{aligned}u_1 &= -\left(1 + k_1\rho/m + k_1^2\right)e_1\\ u_2 &= -\left(1 + k_2\rho/m + k_2^2\right)e_3\end{aligned} \tag{33}$$

where $k = k_1 = k_2$ is a suitable control gain and $0 < k < \rho/m$. The control gain can be selected as $k = k_0 m/\rho$ such that since $\rho \gg m$[1] for the microparticles in the range of 1–10 μm diameter, one can simplify equation (33) as

$$u_1 = -(1 + k_0)(x_1 - x_r)\ ,\quad u_2 = -(1 + k_0)(y_1 - y_r) \tag{34}$$

where k_0 is a positive real number. Taking together, the proposed nonlinear controller is composed of equations (31), (32) and (34).

Experimental control results

In practical experiments, many elements, such as magnetic saturation, fluid viscosity, position of the electromagnets, background noise of the captured images and distance between microparticle and pole tips, have influence on the control performance. The laboratory temperature is kept around 21 °C, and the electromagnet material temperature is limited with 35 °C during studies. First, from the experimental data, a model validation test is performed and the model variables are determined as $k_{fm} = 2.41 \times 10^{-13}\ \mathrm{N/A^2}$ and $\rho = 2.1 \times 10^{-7}\ \mathrm{Ns/m}$. Then, the control experiments are performed using the linear and nonlinear controllers. The experimental results of the linear controller are given in Figures 6–12. Since the characteristic equation is $ms^2 + \rho s + k_{px} = 0$ in equation (18), and since

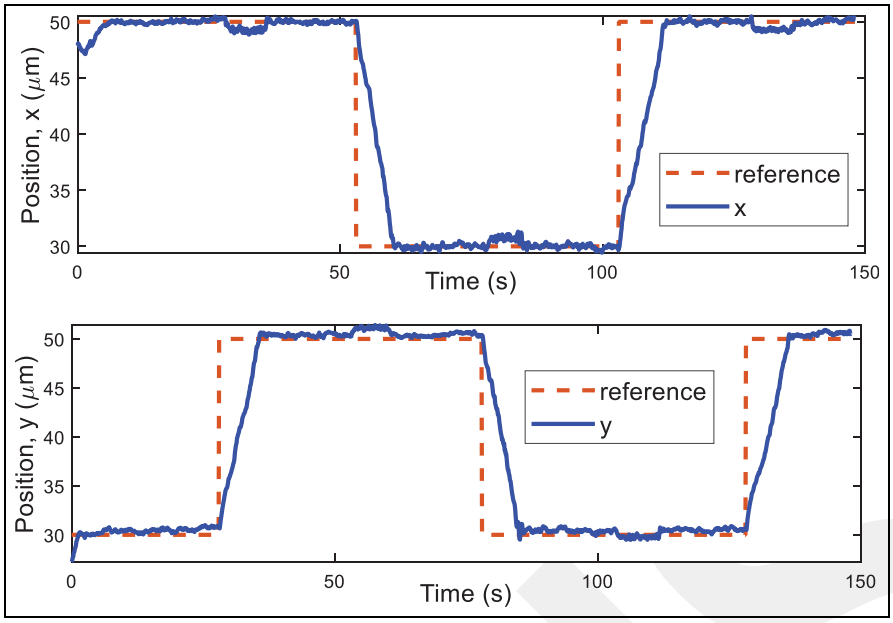

Figure 7. The time responses of the linear controller for the micromanipulator system.

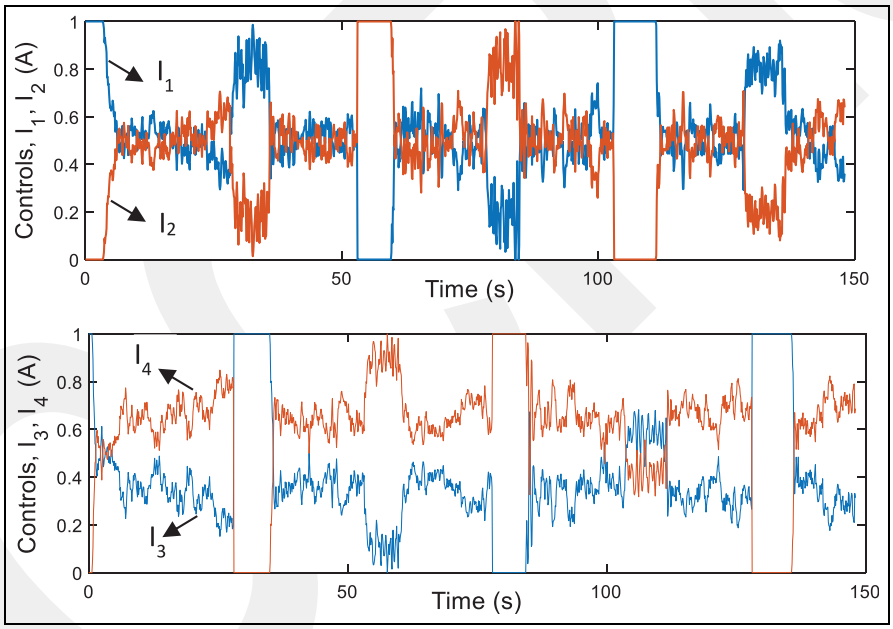

Figure 8. The time responses of control current inputs.

$\rho \gg m$, the dominant pole of the closed-loop system under linear controller can be found approximately as $-k_{px}/\rho$. This means that for a desired settling time $\tau_d = 0.25\,\text{s}$, the control gain is found to be $k_{px} = k_{py} = \rho/\tau_d = 0.8 \times 10^{-6}\,\text{N/m}$. The control currents are restricted around 1 A to eliminate the magnetic saturation of the core materials. The current restriction results in about 25 pN magnetic force generation on the magnetic microparticle and 5μm/s particle velocity around the center of the workspace. Figure 6 shows the phase portrait of the system states x_1 and y_1. The corners of the square shape are the constant reference values (i.e. (50, 30), (50, 50), (30, 50) and (30, 30) are the reference coordinates (in μm)). Figure 7 illustrates the time responses of the linear controllers. The controlled system settles around 1 s as expected due to the design requirements and does not exhibit an overshoot. It is clear from Figures 6 and 7 that the system

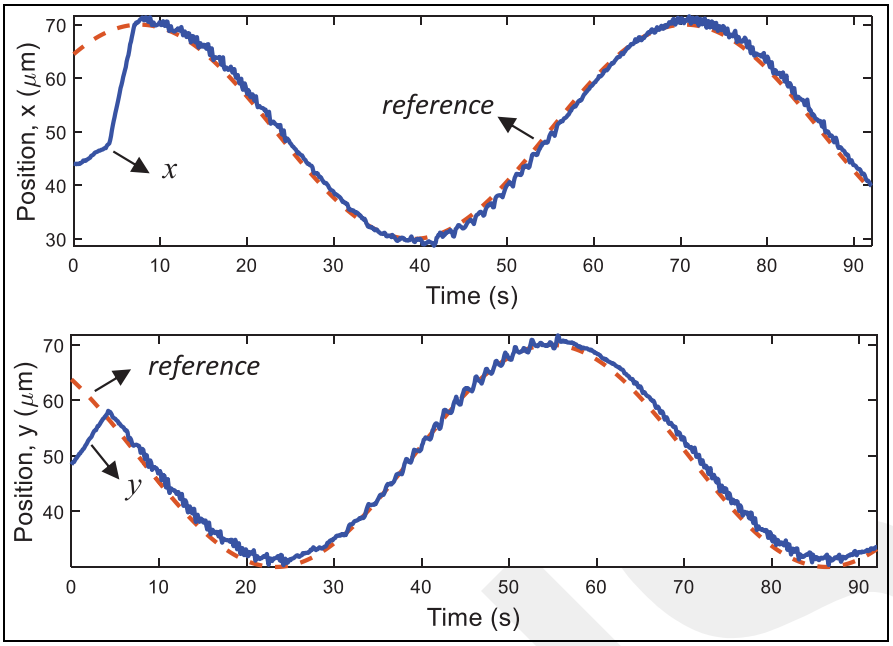

Figure 9. The time responses of the linear controller for the micromanipulator system under sinusoidal (time-varying) reference signals.

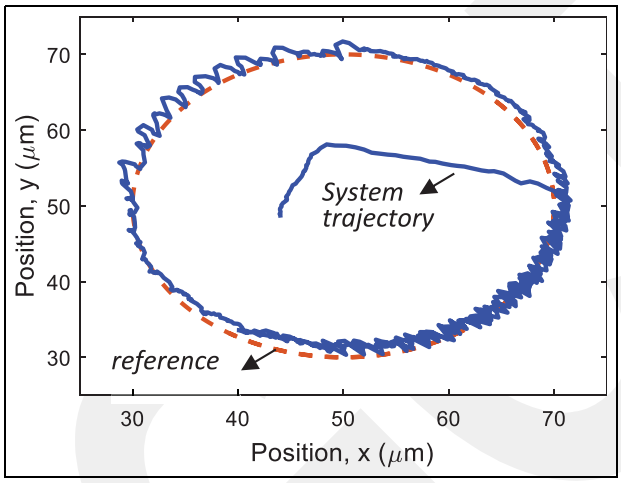

Figure 10. The phase-plane portrait of the system trajectories for sinusoidal (time-varying) reference signals.

trajectories follow the references satisfactorily, and during steady state, the error stays around zero. Because of the effects of the Brownian noise force and measurement error, around $\pm 0.25\,\mu$m, fluctuations on the position signals are observed. Figure 8 displays the control currents. The currents reach the maximum values during the step reference variations from one set value to another, but at steady-state conditions, the currents have values around 0.5 A. One can notice that step changes on the reference signals causes small tracking errors around $\pm 0.5\mu$m. This occurs because the interactions between the magnetic fields of the electromagnets result in a slight movement of the electromagnets. This effect can be reduced by fixing the electromagnets around the workspace. Figures 9–12 display the performance of the linear controller under time-varying (sinusoidal) reference inputs, and again robust tracking results are seen.

The experimental results of the nonlinear controller are provided in Figures 13–15. Since the characteristic equation of the closed-loop system under nonlinear controller is $ms^2 + \rho s + k_c(1 + k_0) = 0$ when substituting equation (20) into equation (19), and since $\rho \gg m$, the dominant pole of the closed-loop system can be found approximately as $-k_c(1 + k_0)/\rho$. This means that for a desired settling time $\tau_d = 0.25$ s, the control gain is found to be $k_c(1 + k_0) = \rho/\tau_d = 0.8 \times 10^{-6}$ N/m. The nonlinear control gains are selected as $k_0 = 0.15$, $k_c = 0.7 \times 10^{-6}$ and $\varepsilon = 0.25$ to have a steady-state current value of 0.5 A. Figure 13 shows the phase portrait of the system states x_1 and y_1. The corners of the square shape, (50, 30), (50, 50), (30, 50) and (30, 30) in μm, are the constant reference values. Figure 14 shows the time response of the nonlinear controller, which provides a non-overshoot transient response with a settling time of 1 s and zero steady-state error. The thermal noise force and measurement noise causes around $\pm 0.2\mu$m fluctuations on the position signals. Again, during the step changes on the reference signals an additional small tracking errors around $\pm 0.4\mu$m occurs because of the interactions between the magnetic fields of the electromagnets. The control currents have values around 0.5 A at steady-state conditions as seen in Figure 15. The control current never reaches zero. Compared with the

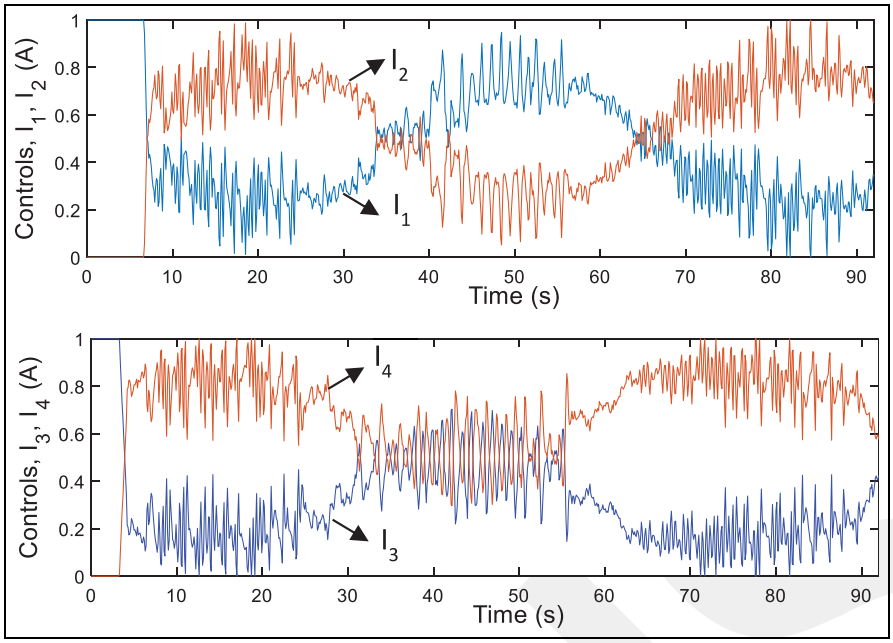

Figure 11. The time responses of control current inputs for sinusoidal references.

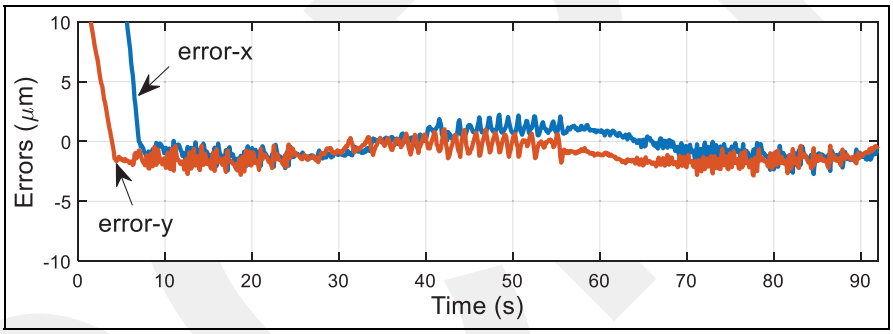

Figure 12. The time responses of tracking errors under time-varying sinusoidal references.

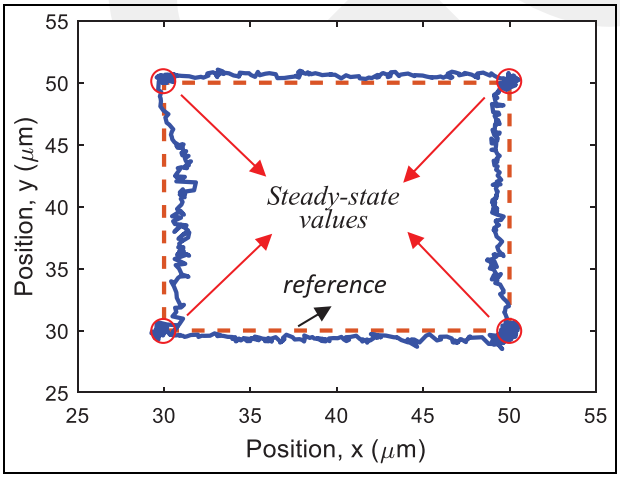

Figure 13. The phase-plane portrait of the system trajectories for step reference signals under nonlinear control. The corners represent the steady-state values.

linear controller (e.g. comparison between Figures 8 and 15), the nonlinear controller provides smoother current control and position signals.

Even though the reference signals are considered as constant during the design of nonlinear controller, the robust performance of the controller is also tested under time-varying reference values. Figures 16–19 are provided to assess the performance of the nonlinear control under sinusoidal references. The proposed nonlinear controller is capable of tracking the time-varying reference values with a very small tracking error as seen in Figure 19. Nonlinear controller has $\pm 2\,\mu$m error while linear controller gives $\pm 2.5\,\mu$m error, so we might say that it is slightly better than the linear controller. In addition, the control currents of the nonlinear controller are smoother than the linear controller (e.g. comparison between Figures 11 and 18). These time-varying tracking results show the satisfying performance and

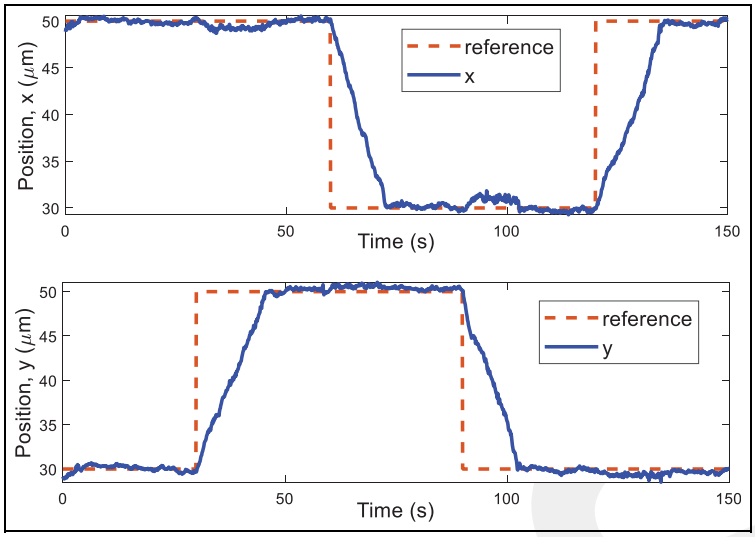

Figure 14. The time responses of the nonlinear controller for the micromanipulator system.

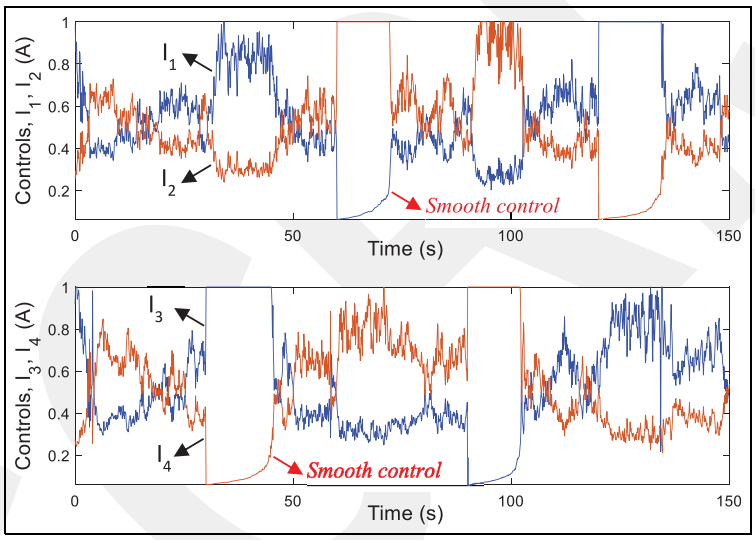

Figure 15. The time responses of control current inputs for nonlinear controller.

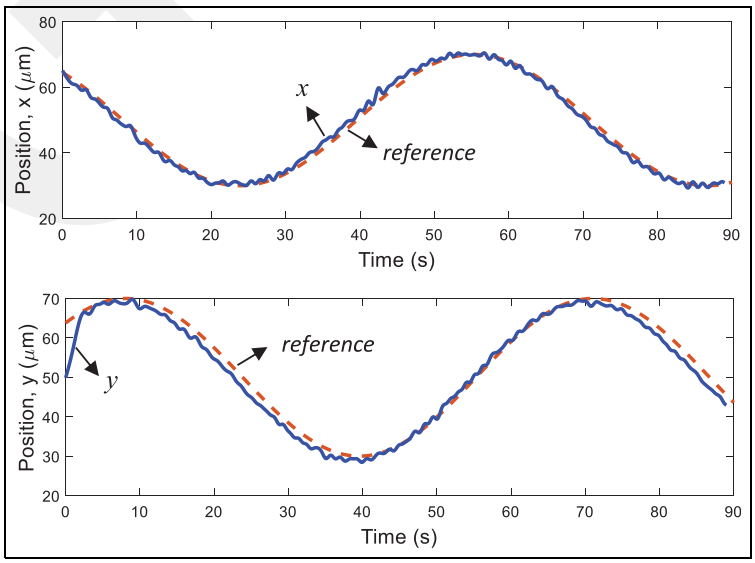

Figure 16. The time responses of the nonlinear controller for the micromanipulator system under sinusoidal reference signals.

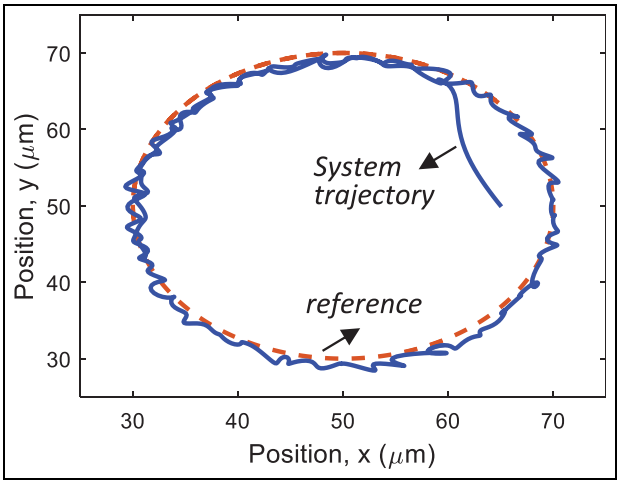

Figure 17. The phase-plane portrait of the system trajectories for sinusoidal reference signals for nonlinear controller.

robustness feature of the proposed nonlinear controller, since it tracks time-varying signals while it is designed for constant references.

Conclusion

In this work, we reported the design, analysis and control of a multipole magnetic micromanipulator for manipulating magnetic microparticles in the range of 1–10 μm in aqueous solution. The magnetic micromanipulator systems have nonlinear dynamics, stability issues and modeling difficulties, which poses control challenges. A current-to-force model for the micromanipulator is derived for controlling purposes. Linear and nonlinear controllers have been proposed as alternative solutions to effectively manipulate a single microparticle. A linear controller is designed using offset current approach, which effectively linearizes the input nonlinearities of the system. A nonlinear

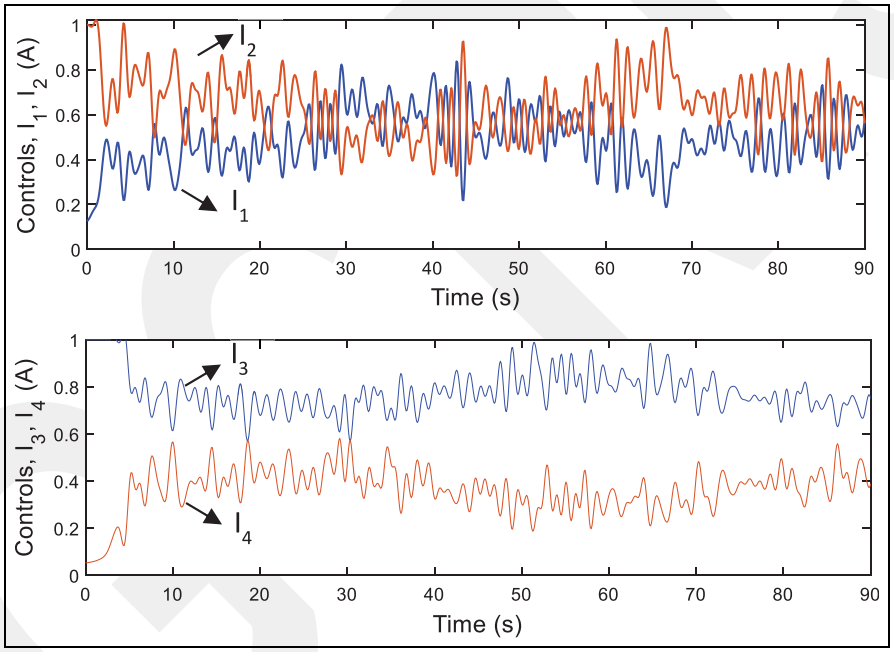

Figure 18. The time responses of nonlinear control current inputs for sinusoidal references.

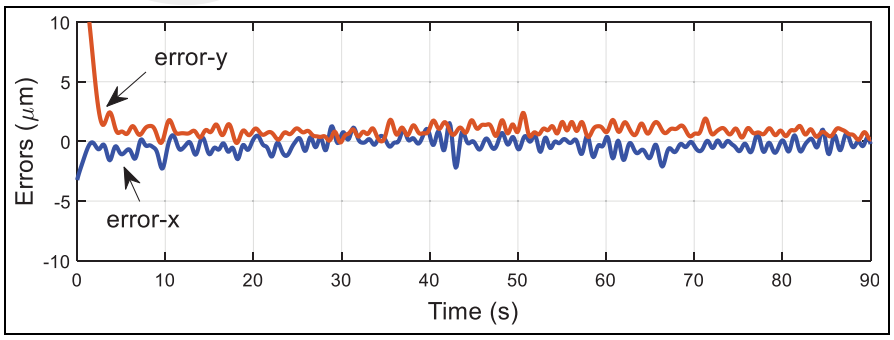

Figure 19. The time responses of tracking errors for nonlinear controller under time-varying sinusoidal references.

controller is also proposed and implemented in this work to smooth the control signals and to improve the control performance. It is demonstrated that the presented controllers ensure global stability of the magnetic micromanipulator system in the workspace limits, and the robustness of the controllers are illustrated through experimental studies. The feedback position signals are acquired from the image-based particle recognition and tracking algorithm to use in feedback controllers. The experimental results of this study show that the controlled magnetic micromanipulator is able to control the magnetic microparticles in a wide range of working space with less than 1 s settling time, non-overshoot response and zero steady-state error. With limited current sources to 1 A, about 25 pN magnetic force is generated on the 4.5 μm diameter magnetic microparticle that is 5 mm away from the electromagnet core tips (i.e. at the center of workspace), and the particle is moved with a velocity of 5 mm/s at the workspace center. The developed, fully automatic controlled micromanipulator can be utilized in single cell or microparticle manipulation–based applications.

Declaration of conflicting interests

The author(s) declared no potential conflicts of interest with respect to the research, authorship and/or publication of this article.

Funding

The author(s) disclosed receipt of the following financial support for the research, authorship and/or publication of this article: This work was supported by Turkish Scientific and Research Council (TUBITAK) under project number 116E168.

ORCID iD

Günyaz Ablay https://orcid.org/0000-0003-2862-6761

References

1. Ablay G, Böyük M and İçöz K. Design, modeling, and control of a horizontal magnetic micromanipulator. *T I Meas Control* 2019; 41: 3190–3198.
2. Achtsnicht S, Schönenborn K, Offenhäusser A, et al. Measurement of the magnetophoretic velocity of different superparamagnetic beads. *J Magn Magn Mater* 2019; 477: 244–248.
3. Elena YF, Mircea I and Ioan A. A bionic study of the magnetic bacteria with applications to the Mecano-magnetic micromanipulators. *Procedia Engineer* 2017; 174: 1128–1139.
4. Long F, Matsuura D and Menq CH. Actively controlled hexapole electromagnetic actuating system enabling 3-D force manipulation in aqueous solutions. *IEEE-ASME T Mech* 2016; 21: 1540–1551.
5. Park IS, Shin JH, Lee YR, et al. On-chip micromanipulation using a magnetically driven micromanipulator with an acoustically oscillating bubble. *Sensor Actuat A: Phys* 2016; 248: 214–222.
6. Vlaminck ID and Dekker C. Recent advances in magnetic tweezers. *Ann Rev Biophys* 2012; 41: 453–472.
7. Yesin KB, Vollmers K and Nelson BJ. Modeling and control of untethered biomicrorobots in a fluidic environment using electromagnetic fields. *Int J Robot Res* 2006; 25: 527–536.
8. Rahman M, Saei AA, Amiri H, et al. Biomedical applications of superparamagnetic nanoparticles in molecular scale. *Curr Org Chem* 2015; 19: 982–990.
9. Fonnum G, Johansson C, Molteberg A, et al. Characterisation of Dynabeads® by magnetization measurements and Mössbauer spectroscopy. *J Magn Magn Mater* 2005; 293: 41–47.
10. Kuznetsov AA. Force acting on a cluster of magnetic nanoparticles in a gradient field: a Langevin dynamics study. *J Magn Magn Mater* 2019; 475: 415–420.
11. Guttula D, Yao M, Baker K, et al. Calcium-mediated protein folding and stabilization of salmonella biofilm-associated protein A. *J Mol Biol* 2019; 431: 433–443.
12. Zhang C, Fu H, Yang Y, et al. The mechanical properties of RNA-DNA hybrid duplex stretched by magnetic tweezers. *Biophys J* 2019; 116: 196–204.
13. Peterson RD, Chen W, Cunningham BT, et al. Enhanced sandwich immunoassay using antibody-functionalized magnetic iron-oxide nanoparticles for extraction and detection of soluble transferrin receptor on a photonic crystal biosensor. *Biosens Bioelectron* 2015; 74: 815–822.
14. Shapiro B, Kulkarni S, Nacev A, et al. Open challenges in magnetic drug targeting. *Wiley Interdiscip Rev Nanomed Nanobiotechnol* 2015; 7: 446–457.
15. Alexiou C, Jurgons R, Schmid RJ, et al. Magnetic drug targeting: biodistribution of the magnetic carrier and the chemotherapeutic agent mitoxantrone after locoregional cancer treatment. *J Drug Target* 2003; 11: 139–149.
16. Wang X, Chen X-Z Alcântara CCJ, et al. MOFBOTS: metal-organic-framework-based biomedical microrobots. *Adv Mater* 2019; 31: 1901592.
17. Agostini A, Kircher M, Do R, et al. MR imaging of the liver (including biliary contrast agents). *Semin Roentgenol* 2016; 51: 308–316.
18. Tietze R, Zaloga J, Unterweger H, et al. Magnetic nanoparticle-based drug delivery for cancer therapy. *Biochem Biophys Res Commun* 2015; 468: 463–470.
19. Obaidat IM, Issa B and Haik Y. Magnetic properties of magnetic nanoparticles for efficient hyperthermia. *Nanomaterials* 2015; 5: 63–89.
20. Mzava O, Taş Z and İçöz K. Magnetic micro/nanoparticle flocculation-based signal amplification for biosensing. *Int J Nanomedicine* 2016; 11: 2619–2631.
21. Farah FH. Magnetic microspheres: a novel drug delivery system. *J Anal Pharmaceut Res* 2016; 3: 00067.
22. Nemati Z, Salili SM, Alonso J, et al. Superparamagnetic iron oxide nanodiscs for hyperthermia therapy: does size matter? *J Alloy Compd* 2017; 714: 709–714.
23. Lu M and Hui H. Delivery of renin inhibitor through mouth mucosa. *Drug Dev Ind Pharm* 1996; 22: 1167–1171.
24. Yukimatsu K, Nozaki Y, Kakumoto M, et al. Development of a trans-mucosal controlled-release device for systemic delivery of antianginal drugs pharmacokinetics and

pharmacodynamics. *Drug Dev Ind Pharm* 1994; 20: 503–534.
25. Plouffe BD, Murthy SK and Lewis LH. Fundamentals and application of magnetic particles in cell isolation and enrichment. *Rep Prog Phys* 2015; 78: 016601.
26. Farzin A, Hassan S, Emadi R, et al. Comparative evaluation of magnetic hyperthermia performance and biocompatibility of magnetite and novel Fe-doped hardystonite nanoparticles for potential bone cancer therapy. *Mater Sci Eng: C Mater Biol Appl* 2019; 98: 930–938.
27. Jiang C, Lionberger TA, Wiener DM, et al. Electromagnetic tweezers with independent force and torque control. *Rev Sci Instrum* 2016; 87: 084304.
28. Neuman KC and Nagy A. Single-molecule force spectroscopy: optical tweezers, magnetic tweezers and atomic force microscopy. *Nat Methods* 2008; 5: 491–505.
29. Xie M, Shakoor A, Shen Y, et al. Out-of-plane rotation control of biological cells with a robot-tweezers manipulation system for orientation-based cell surgery. *IEEE T Biomed Eng* 2019; 66: 199–207.
30. Bhatt G and Bhattacharya S. Biosensors on chip: a critical review from an aspect of micro/nanoscales. *J Micromanuf*. Epub ahead of print 17 June 2019. DOI: 10.1177/2516598419847913.
31. Kriegel F, Ermann N and Lipfert J. Probing the mechanical properties, conformational changes, and interactions of nucleic acids with magnetic tweezers. *J Struct Biol* 2017; 197: 26–36.
32. Gosse C and Croquette V. Magnetic tweezers: micromanipulation and force measurement at the molecular level. *Biophys J* 2002; 82: 3314–3329.
33. Strick TR, Allemand JF, Bensimon D, et al. Behavior of supercoiled DNA. *Biophys J* 1998; 74: 2016–2028.
34. Dekker NH, Viard T, de La, Tour CB, et al. Thermophilic topoisomerase I on a single DNA molecule. *J Mol Biol* 2003; 329: 271–282.
35. Fountain TWR, Kailat PV and Abbott JJ. Wireless control of magnetic helical microrobots using a rotating-permanent-magnet manipulator. In: *Proceedings of the 2010 IEEE international conference on robotics and automation*, Anchorage, AK, 3–7 May 2010, pp.576–581. New York: IEEE.
36. Prass M, Jacobson K, Mogilner A, et al. Direct measurement of the lamellipodial protrusive force in a migrating cell. *J Cell Biol* 2006; 174: 767–772.
37. Litvinov RI, Shuman H, Bennett JS, et al. Binding strength and activation state of single fibrinogen-integrin pairs on living cells. *Proc Natl Acad Sci USA* 2002; 99: 7426–7431.
38. Hosu BG, Jakab K, Bánki P, et al. Magnetic tweezers for intracellular applications. *Res Sci Instrum* 2003; 74: 4158–4163.
39. Lucarini G, Iacovacci V, Ricotti L, et al. Magnetically driven microrobotic system for cancer cell manipulation. In: *Proceedings of the 2015 37th annual international conference of the IEEE engineering in medicine and biology society (EMBC)*, Milan, 25–29 August 2015, pp.3631–3634. New York: IEEE.
40. Chen X-Z, Hoop M, Mushtaq F, et al. Recent developments in magnetically driven micro- and nanorobots. *Appl Mater Today* 2017; 9: 37–48.
41. Lee S, Kim S, Kim S, et al. A capsule-type microrobot with pick-and-drop motion for targeted drug and cell delivery. *Adv Healthc Mater* 2018; 7: e1700985.
42. Eroğlu Y and Ablay G. Cascade sliding mode-based robust tracking control of a magnetic levitation system. *Proc IMechE, Part I: J Systems and Control Engineering* 2016; 230: 851–860.
43. Davis JR. *ASM specialty handbook: nickel, cobalt, and their alloys*. Peoria, IL: ASM International, 2001.
44. Hejazian M, Li W and Nguyen N-T. Lab on a chip for continuous-flow magnetic cell separation. *Lab Chip* 2015; 15: 959–970.
45. Happel J and Brenner H. *Low Reynolds number hydrodynamics: with special applications to particulate media*. The Hague: Springer, 1983.
46. Nguyen N-T. Micro-magnetofluidics: interactions between magnetism and fluid flow on the microscale. *Microfluid Nanofluid* 2012; 12: 1–16.
47. Shevkoplyas SS, Siegel AC, Westervelt RM, et al. The force acting on a superparamagnetic bead due to an applied magnetic field. *Lab Chip* 2007; 7: 1294–1302.
48. Gittes F and Schmidt CF. Thermal noise limitations on micromechanical experiments. *Eur Biophys J* 1998; 27: 75–81.
49. Kim M and Zydney AL. Effect of electrostatic, hydrodynamic, and Brownian forces on particle trajectories and sieving in normal flow filtration. *J Colloid Interf Sci* 2004; 269: 425–431.